Article

Structural and Mechanistic Basis of an Oxepin-CoA Forming Isomerase in Bacterial Primary and Secondary Metabolism

Melanie Spieker, Raspudin Saleem-Batcha, and Robin Teufel

ACS Chem. Biol., **Just Accepted Manuscript** • DOI: 10.1021/acschembio.9b00742 • Publication Date (Web): 05 Nov 2019

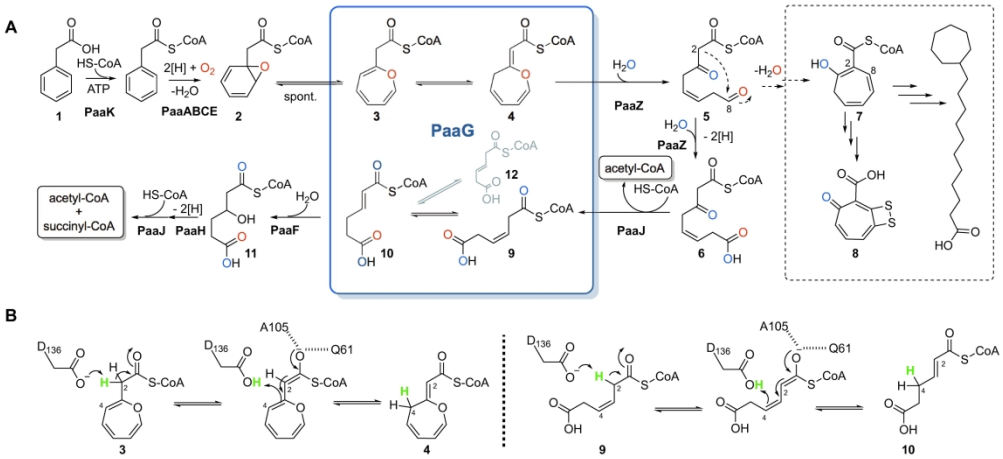

Figure 1. (A) Bacterial phenylacetic acid (1) catabolic pathway (2), see text for details. PaaG catalyzes two isomerization steps of structurally-distinct CoA-esters 2/3 and 9, which affords 4 and 10, respectively (purple box). In addition, non-native substrate 12 (in grey) is converted to 10 by PaaG. If labile 5 is not immediately oxidized to 6, spontaneous condensation (indicated by dashed arrows) generates 7 that is likely the sought precursor for primary and secondary metabolites (dashed box). Ultimately, 1 is degraded to two acetyl-CoA and one succinyl-CoA. The red and blue colored oxygen atoms derive from O2 and H2O, respectively. (B) Proposed PaaG catalytic mechanism for both native substrates 3 (tautomer 2 not shown) and 9 involving the catalytic aspartate side chain and thioester enolate transition states stabilized by hydrogen bonding (residue numbering from T. thermophilus). The shuttled proton is highlighted in green.

288x131mm (300 x 300 DPI)

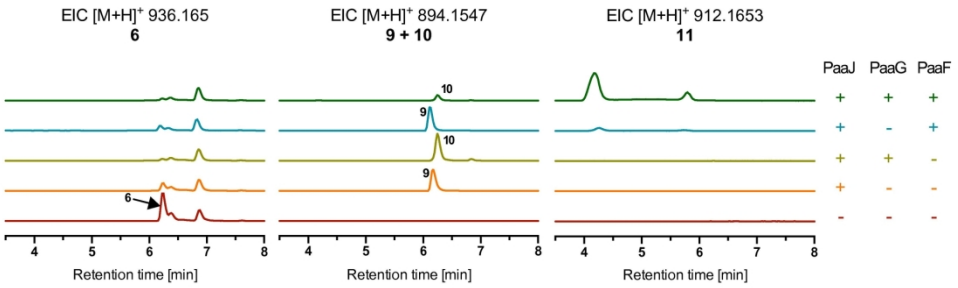

Figure 2. UPLC-HRMS data of enzyme reactions with 6 as substrate. Traces with the same color belong to the same assay (respective enzyme compositions shown to the right). Shown are the extracted ion chromatograms (EICs) for [M+H]+ of 936.165 (compound 6), [M+H]+ of 894.155 (compounds 9 and 10) and [M+H]+ of 912.165 (compound 11), respectively. Only in presence of PaaGPY2, 10 is formed in significant amounts, thus verifying the Δ3,Δ2-enoyl-CoA isomerase activity of PaaG. Trace amounts of 11 formed in the absence of PaaG can be explained by the known low isomerase side activity of enoyl-CoA hydratases (PaaF). Note that 9 and 10 have identical masses but slightly different retention times and can be further distinguished by the characteristic UV-Vis spectra (Supplementary Figure 2). If not further converted, unstable 9 spontaneously decomposes.

176x54mm (300 x 300 DPI)

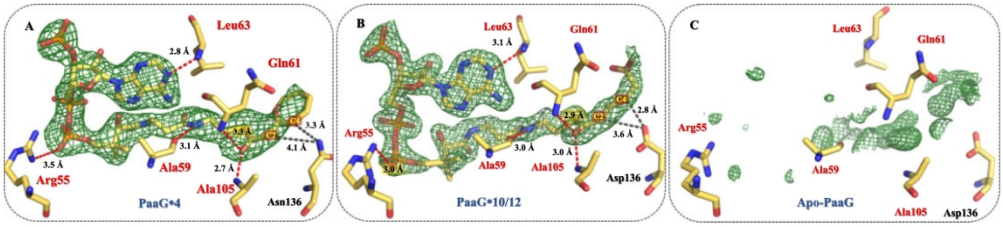

Figure 3. Polder OMIT maps (contoured at 3σ above the mean) of (A) PaaGTT-D136N•4 (PDB ID: 6SLA), (B) PaaGTT•10/12 (PDB ID: 6SLB), and (C) apo-PaaGTT (PDB ID: 6SL9). The unbiased maps allowed placement of the ligands within the electron density. For unsoaked apo-PaaGTT, water molecules and spurious density could be observed. Note that the distance and orientation of residue 136 to the C2 and C4 atoms of the ligand in 6SLA differs due to replacement of the catalytic aspartate residue with asparagine, which adopts a different conformation.

292x66mm (300 x 300 DPI)

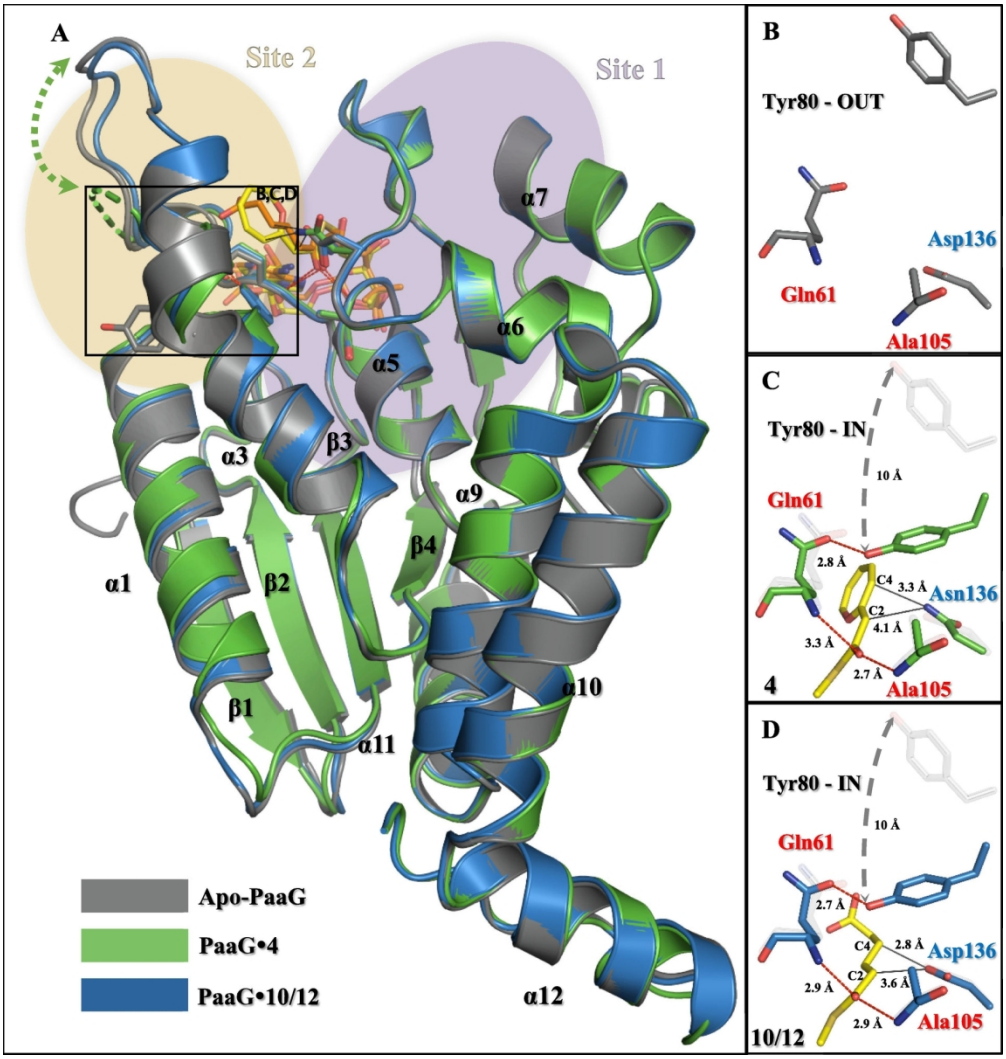

Figure 4. Overall structure and active site of PaaGTT. (A) Superposition of apo-PaaGTT (grey), PaaGTT-D136N•4 chain A (green), PaaGTT•10/12 (blue). (B, C, D) Inlets showing the respective enlarged active sites. Catalytic residues and ligands are represented as stick models. Distances, e.g., between the catalytic Asp136 and the C2 and C4 atoms of the ligands are indicated in Å. The mobile Tyr80 closes the active site upon substrate binding and expels water. To accommodate 4, loop β3-α3 opens up and thereby provides space for the bulky ring.

162x170mm (300 x 300 DPI)

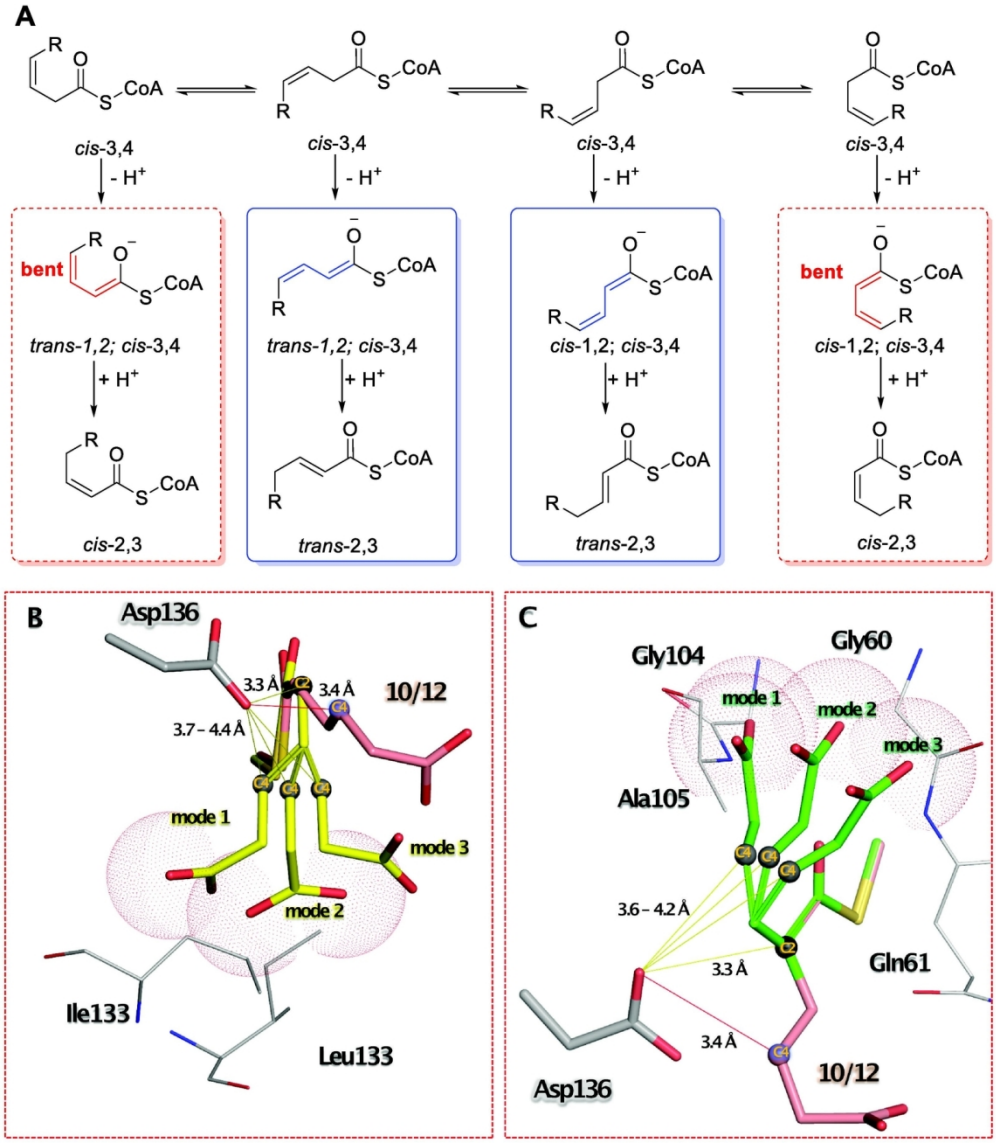

Figure 5. (A) Possible conformations of PaaG's native substrate 9 in enzyme free environment (top). The thioester enolates, following deprotonation, represent the transition states (middle), which are converted to the products (bottom). If the transition state adopts a bent conformation (red boxes), the undesired cis-2,3 product would be formed rather than the observed trans-2,3 (blue boxes). R = CH2COOH. (B, C) PaaGTT suppresses the bent conformation of the transition state through a confined active site, thereby steering the exclusive formation of trans-2,3-didehydroadipoyl-CoA (10). Modeled bent cis-1,2, cis-3,4 transition state binding-modes are shown as yellow sticks (B) and modeled bent trans-1,2, cis-3,4 transition state binding-modes as green sticks (C). Both transition state models are aligned along the CoA-moieties and C1-C2 axes with the experimentally observed 10/12 (pink sticks). Red spheres represent steric clashes of transition states with the protein. The C2 and C4 atoms are highlighted as spheres with indicated distances to the catalytic D136 side chain.

135x154mm (300 x 300 DPI)

Structural and Mechanistic Basis of an Oxepin-CoA Forming Isomerase in Bacterial Primary and Secondary Metabolism

Authors: Melanie Spieker[†,‡,§], Raspudin Saleem-Batcha[†,‡,§], & Robin Teufel[†,‡,*]

Affiliations:

[†]ZBSA, Center for Biological Systems Analysis, University of Freiburg, 79104 Freiburg, Germany.

[‡]Faculty of Biology, University of Freiburg, 79104 Freiburg, Germany.

[§]These authors contributed equally

[*]Correspondence: robin.teufel@zbsa.uni-freiburg.de

Abstract

Numerous aromatic compounds are aerobically degraded in bacteria via the central intermediate phenylacetic acid (paa). In one of the key steps of this widespread catabolic pathway, 1,2-epoxyphenylacetyl-CoA is converted by PaaG into the heterocyclic oxepin-CoA. PaaG thereby elegantly generates an α,β-unsaturated CoA ester that is predisposed to undergo β-oxidation subsequent to hydrolytic ring-cleavage. Moreover, oxepin-CoA serves as precursor for secondary metabolites (e.g., tropodithietic acid) that act as antibiotics and quorum sensing signals. Here we verify that PaaG adopts a second role in aromatic catabolism by converting *cis*-3,4-didehydroadipoyl-CoA into *trans*-2,3-didehydroadipoyl-CoA and corroborate a Δ^3,Δ^2-enoyl-CoA isomerases-like proton shuttling mechanism for both distinct substrates. Biochemical and structural investigations of PaaG reveal active site adaptations to the structurally different substrates and provide detailed insight into catalysis and control of stereospecificity. This work elucidates the mechanism of action of unusual isomerase PaaG and sheds new light on the ubiquitous enoyl-CoA isomerases of the crotonase superfamily.

Aromatic compounds are highly abundant in nature and serve as important carbon and energy sources for microorganisms. Commonly, peripheral pathways convert structurally diverse aromatics into a small number of central intermediates such as benzoic acid or phenylacetic acid (paa, compound **1**, Figure 1A) before further degradation via central pathways takes place *(1)*. Depending on the availability of dioxygen (O_2), different strategies are employed to overcome the high resonance energy of the aromatic ring *(1)*. Under aerobic conditions, ring activation through hydroxylation is followed by oxygenolytic ring-cleavage. In contrast, in the absence of O_2, aromatics such as benzoic acid are activated by CoA thioester formation and subsequently reduced, before hydrolytic ring-cleavage yields open-chain CoA-thioesters that are degraded via β-oxidation-like steps *(1)*. In addition, "hybrid strategies" (likely preferably employed under microaerobic conditions) combine features of both paradigms, i.e. CoA-thioester formation, ring activation through oxygenation (i.e. epoxidation), hydrolytic ring cleavage, and β-oxidation-like steps *(2–8,1,9)*. For instance, numerous phylogenetically diverse bacteria (e.g., *Escherichia coli* K-12 or *Thermus thermophilus*) and some archaea employ a hybrid pathway for degradation of **1** *(2,10,11,6,3,7)*, which is also relevant for virulence of *Burkholderia cenocepacia* in cystic fibrosis *(12)* (Figure 1A).

In the phenylacetic acid degradation pathway (2), **1** is first ligated with coenzyme A by PaaK to phenylacetyl-CoA *(13,2)* and then epoxidation by the diiron-dependent multicomponent monooxygenase PaaABCE results in 1,2-epoxyphenylacetyl-CoA (**2**) *(10,2,14)*. Isomerase PaaG next produces an α,β-unsaturated CoA-thioester motif by isomerizing **2** (or its spontaneously formed tautomer 2-(oxepin-yl)acetyl-CoA (**3**)) into the

unusual enolether (*Z*)-2-(oxepin-2(3H)-ylidene)acetyl-CoA ("oxepin-CoA", **4**), which is prone to undergo hydrolytic ring cleavage catalyzed by the hydratase domain of the bifunctional fusion protein PaaZ *(2,11)*. The resulting open-chain aldehyde (**5**) is further oxidized to the stable 3-oxo-5,6-didehydrosuberoyl-CoA (**6**) by the NAD(P)$^+$-dependent aldehyde dehydrogenase domain of PaaZ. If not directly oxidized, highly reactive **5** spontaneously undergoes rapid intramolecular aldol condensation followed by dehydration (Knoevenagel condensation), thereby affording 2-hydroxycyclohepta-1,4,6-triene-1-carboxyl-CoA (**7**) featuring a seven-membered carbon cycle *(11)*. Compound **7** represents a shunt product of the catabolic pathway, but most likely serves as precursor for unusual ω-cycloheptyl fatty acids *(15)* as well as tropone-based secondary metabolites including, e.g., tropoditheitic acid *(16–25)* (**8**) or various roseobacticides (Figure 1A) *(26–28)*. In contrast, further catabolism of **6** proceeds via β-oxidation-like steps catalyzed by β-ketothiolase (PaaJ) *(2)* that generates acetyl-CoA and presumably *cis*-3,4-didehydroadiypl-CoA (**9**), which is further isomerized to *trans*-2,3-didehydroadiypl-CoA (**10**). Final β-oxidation-like steps are catalyzed by enoyl-CoA hydratase (PaaF), alcohol dehydrogenase (PaaH) *(2)*, and once more PaaJ *(2,29)*, in total producing two acetyl-CoA and one succinyl-CoA (Figure 1A) *(2)*.

PaaG and PaaF both belong to the enoyl-CoA hydratase/isomerase ("crotonase") superfamily *(2,30,31)* that comprise well-investigated enzymes *(30,32–37)*. As a universal feature during catalysis, a negative charge develops in the transition state in the form of a thioester enolate, which is stabilized by a dedicated pocket (i.e. the "oxyanion hole") in the active site via hydrogen-bonding interactions. Hence all enzymes of this superfamily strictly depend on CoA-thioester substrates, while the attached acyl groups may differ *(30)*. Enoyl-CoA hydratases employ two conserved acidic amino acid residues for the activation and incorporation of water at the β–position *(32)*, whereas isomerases apparently utilize only a single acidic side-chain (Glu or Asp) as proton shuttle *(34–36)*. In the case of PaaG, a similar mechanism can be envisaged and a second PaaG-mediated isomerization reaction in the pathway, i.e. the conversion of **9** to **10**, has been proposed before without experimental validation *(2)*. Previously, PaaG from *Pseudomonas* sp. Y2 (henceforth referred to as PaaG^{PY2}) was shown to catalyze the isomerization of **2**/**3** to **4** by *in vitro* assays, mass spectrometry including ^{18}O-labelling, as well as nuclear magnetic resonance (NMR) studies with ^{13}C-labelled precursors *(2)*. In addition, crystal structures of apo-PaaG from *Thermus thermophilus* (PaaG^{TT}) *(38)* and apo-PaaG in complex with apo-PaaF from *E. coli K-12 (31)* were reported previously. In this work, we characterize PaaG in detail and provide evidence for a Δ^3,Δ^2-enoyl-CoA isomerase-like activity by combining mechanistic and structural studies with native substrates, thereby confirming PaaG's unusual dual function, while providing general insight into structural requisites for isomerase catalysis.

Figure 1. (**A**) Bacterial phenylacetic acid (**1**) catabolic pathway *(2)*, see text for details. PaaG catalyzes two isomerization steps of structurally-distinct CoA-esters **2**/**3** and **9**, which affords **4** and **10**, respectively (purple box). In addition, non-native substrate **12** (in grey) is converted to **10** by PaaG. If labile **5** is not immediately oxidized to **6**, spontaneous condensation (indicated by dashed arrows) generates **7** that is likely the sought precursor for primary and secondary metabolites (dashed box). Ultimately, **1** is degraded to two acetyl-CoA and one succinyl-CoA. The red and blue colored oxygen atoms derive from O_2 and H_2O, respectively. (**B**) Proposed PaaG catalytic mechanism for both native substrates **3** (tautomer **2** not shown) and **9** involving the catalytic aspartate side chain and thioester enolate transition states stabilized by hydrogen bonding (residue numbering from *T. thermophilus*). The shuttled proton is highlighted in green.

Results and Discussion

PaaG Catalyzes Two Distinct Isomerization Steps in Phenylacetatic Acid Catabolism

The unusual conversion of **2**/**3** to **4** catalyzed by PaaG can be envisaged by a Δ^3,Δ^2-enoyl-CoA isomerase-like mechanism, consistent with amino acid sequence-based functional

predictions (Figure 1B). Typically, Δ^3,Δ^2-enoyl-CoA isomerases catalyze the conversion of enoyl-CoA esters with *cis*-3,4 or *trans*-3,4 configuration into *trans*-2,3-enoyl-CoAs. Previously, we speculated that PaaG may thus also be involved in a further downstream step by isomerizing **9** to **10**, albeit other candidates (e.g., PaaJ) could not be ruled out *(2)*. To further investigate this, we first sought to acquire the proposed PaaG substrate, i.e. 3,4-didehydroadiypl-CoA (**9**) that is produced via PaaJ-mediated thiolytic cleavage of precursor **4** and most likely retains the *cis*-configuration of the double bond (Figure 1A). As *cis*-3,4-didehydroadipate cannot be purchased commercially, we first attempted to produce **9** enzymatically. However, **9** proved to be highly unstable during purification, most likely due to CoA-ester elimination via spontaneous intramolecular acid anhydride formation and could not be isolated in sufficient amounts for enzymatic assays. Instead, we enzymatically generated and purified the adequately stable PaaZ product **6**, which was then used as substrate for *in vitro* coupled enzyme assays to investigate the postulated Δ^3,Δ^2-isomerization step that affords **10**. The assays contained **6**, HS-CoA, as well as different combinations of PaaJ, PaaG and enoyl-CoA hydratase PaaF (that converts **10** into 3-hydroxyadipoyl-CoA (**11**)) (Figure 2). Indeed, these experiments confirmed that $PaaG^{PY2}$ catalyzes the formation of **10**, as verified by ultra performance liquid chromatography high-resolution mass spectrometry (UPLC-HRMS) (Figure 2).

Figure 2. UPLC-HRMS data of enzyme reactions with **6** as substrate. Traces with the same color belong to the same assay (respective enzyme compositions shown to the right). Shown are the extracted ion chromatograms (EICs) for $[M+H]^+$ of 936.165 (compound **6**), $[M+H]^+$ of 894.155 (compounds **9** and **10**) and $[M+H]^+$ of 912.165 (compound **11**), respectively. Only in presence of $PaaG^{PY2}$, **10** is formed in significant amounts, thus verifying the Δ^3,Δ^2-enoyl-CoA isomerase activity of PaaG. Trace amounts of **11** formed in the absence of PaaG can be explained by the known low isomerase side activity of enoyl-CoA hydratases (PaaF). Note that **9** and **10** have identical masses but slightly different retention times and can be further distinguished by the characteristic UV-Vis spectra (Supplementary Figure 2). If not further converted, unstable **9** spontaneously decomposes.

In addition, **6** was used as substrate for coupled enzyme assays to estimate the specific activity by UPLC-HRMS for the conversion of **9** into **10** for both $PaaG^{PY2}$ and $PaaG^{TT}$ (Table 1). Because of the instability of the native substrate **9**, we chemically synthesized and purified isomer *trans*-3,4-didehydroadipoyl-CoA (**12**) (for details, see experimental section) for detailed structural and further mechanistic studies. As expected, **12** proved to be significantly more stable and was converted to the same product **10**, as verified by UPLC-HRMS (Supplementary Figure 1). The kinetic parameters for the $PaaG^{PY2}$/$PaaG^{TT}$-mediated conversion of **12** into **10** were then determined spectrophotometrically at 30 °C (Supplementary Figure 2 and Table 1). In addition, we determined the specific activities for the second native substrate **2**/**3**. For that, HPLC assays were employed due to the instability of **2** and because spectrophotometric assays were impeded by NADPH, [2Fe-2S]-clusters, and FAD (required by or part of PaaABCE) (Supplementary Figure 3). Overall, $PaaG^{TT}$ appeared to be more adapted to the conversion of the bulky ring-substrate **2**/**3**, whereas $PaaG^{PY2}$ readily converted both linear substrates (**9** & **12**) as well as **2**/**3**. Interestingly, chemically synthesized 2-cyclohexenylacetyl-CoA that is structurally similar to **2**/**3** was not accepted by either enzyme, as determined spectrophotometrically, by HPLC, and by X-ray crystallography (see below). The enzyme kinetics are summarized in Table 1.

A Catalytic Aspartate Side Chain Acts as Proton Relay in PaaG

Δ^3,Δ^2-enoyl-CoA isomerases are proposed to shuttle a proton between C4 and C2 of the respective enoyl-CoA substrates in a reversible reaction (Figure 1B). In PaaG, an aspartate side chain (D136) is found in the position of the proposed catalytic residue *(2,31,38)*. To further examine the role of D136, we constructed a $PaaG^{TT}$-D136N variant, which was crystallized along with the wild type (wt). The overall structure of $PaaG^{TT}$-D136N was highly similar to

PaaG^{TT} wt and showed no significant changes, as further confirmed using circular dichroism (CD) spectroscopy (that was also conducted for other enzyme variants discussed below) (Supplementary Figure 4). As expected, PaaG^{TT}-D136N functionality was drastically affected, allowing the enzyme to operate at < 0.1 % relative activity for the conversion of **2** to **4** compared to PaaG^{TT} wt (Table 1), while activity for **12** was completely abolished, thus strongly supporting a catalytic role for D136. This critical function of D136 was further corroborated by the complex structures of PaaG^{TT} wt and PaaG^{TT}-D136N with native ligands (see crystallography section below).

Table 1. Overview of PaaG kinetic parameters. Parameters for PaaG^{TT} wt (and variants) and PaaG^{PY2} were determined for 1,2-epoxyphenylacetyl-CoA (**2**), *trans*-3,4-didehydroadipoyl-CoA (**12**) and 2-cyclohexenylacetyl-CoA. Different methods for measurement were applied: [1]: measured in coupled assay by HPLC; [2]: measured with spectrophotometer; [3]: measured by UPLC-MS. Abbreviations: n.d.: (activity) not detected; -: not measured.

Kinetics of PaaG^{TT} and PaaG^{PY2}

		1,2-epoxyphenyl-acetyl-CoA (**2**) [1]	*cis*-3,4-didehydro-adipoyl-CoA (**9**) [3]	*trans*-3,4-didehydroadipoyl-CoA (**12**) [2]				2-cyclohexenyl-acetyl-CoA [1 & 2]
	Enzyme form	specific activity in U mg^{-1}	specific activity in U mg^{-1}	specific activity in U mg^{-1}	K_m in µM	k_{cat} in s^{-1}	Catalytic efficiency in s^{-1} µM^{-1}	specific activity in U mg^{-1}
PaaG^{TT}	wild type	138 ± 11	3 ± 1	(7.6 ± 0.9) 10^{-3}	564 ± 149	(3.5 ± 0.4) 10^{-3}	(6 ± 3) 10^{-6}	n.d.
	variant Y80F	99 ± 6	-	(9.1 ± 0.6) 10^{-4}	123 ± 23	(4.5 ± 0.3) 10^{-4}	(4 ± 1) 10^{-6}	-
	variant D136N	0.05 ± 0.01	-	n.d.	n.d.	n.d.	n.d.	-
	variant Y80F/D136N	0.15 ± 0.01	-	n.d.	n.d.	n.d.	n.d.	-
PaaG^{PY2}	wild type	182 ± 10	105 ± 16	116 ± 4	142 ± 13	(60 ± 0.1) 10^{-3}	(4 ± 2) 10^{-4}	n.d.

Structural Elucidation of PaaG in Complex with Native Ligands

To gain insight into the substrate binding mode and catalytic mechanism, we next attempted to crystallize PaaG^{TT} with the native ligands. After modification of previously reported conditions, diffracting polygonal shaped crystals of the PaaG^{TT} wildtype and PaaG^{TT}-D136N were obtained. Co-crystallization with native ligands, however, did not meet with success. Soaking of PaaG^{TT} crystals with enzymatically prepared **9** also failed due to its instability. Hence, we focused our efforts on crystal soaking with more stable **4** and **12** (that can be converted in the PaaG active site to the on-pathway product **10**). In addition, 2-cyclohexenylacetyl-CoA was used that structurally resembles **4** (Table 1). For soaking experiments with **4**, the PaaG^{TT}-D136N variant was employed because of the reversibility of isomerization of **2** to **4** and the innate instability of **2**. Compared to the previously published apo-PaaG^{TT} (form I; PDB ID: 3HRX *(38)*), we obtained two distinct crystal forms II and III of PaaG^{TT}. Molecular replacement provided phasing in the cubical $P2_13$ space group with one chain in the asymmetric unit (form II for apo-PaaG^{TT} and complex structures of PaaG^{TT}·**10**/**12**) and a monoclinic $P2_1$ space group with six chains in the asymmetric unit (form III for PaaG^{TT}-D136N·**4**) (Table 2). According to PISA *(40)* prediction, both the apo and complex structures (forms II and III) form a stable homotrimeric biological assembly, consistent with previous reports *(38)*. Data statistics and refinements are shown in Supplementary Table 1.

Table 2. Overview of obtained crystal structures of PaaG^{TT} (homotrimeric in its biologically active form) and local displacements.

Structures	PDB codes	Crystal Forms	Space group	Resolution (Å)	Ligand	Monomers in asu	Oligomeric state	loop β3-α3	Tyr80 (IN or OUT)	Distance: Tyr80-Asp136/Asn136 (in Å)
Apo-PaaG^{TT} (this study)	6SL9	II	$P2_13$	1.27	no	1	**homotrimer**	**O**	**OUT**	13.1
PaaG^{TT}·**10/12** (this study)	6SLB	II	$P2_13$	1.88	**10/12**	1	**homotrimer**	**O**	**IN**	5.6
PaaG^{TT}-D136N·**4** (this study) **(chains A-F)**	6SLA	III	$P2_1$	2.55	**4**	6	**homotrimer**	A: **Ø** B: **Ø** C: **Ø** D: **Ø** E: **Ø** F: **Ø**	A: **IN** B: **IN** C: **IN** D: **IN** E: **IN** F: **IN**	5.9 5.8 5.6 5.5 6.4 5.7
*Apo-PaaG^{TT} **(chains A-F)**	3HRX	I	$P2_12_12_1$	1.85	no	6	**homotrimer**	A: **O** B: **O** C: **O** D: **O** E: **O** F: **Ø**	A: **IN** B: **OUT** C: **OUT** D: **OUT** E: **OUT** F: **IN**	6.4 12.9 13.0 13.1 13.1 6.1

(Abbreviations/symbols: **asu** – asymmetric unit; **O** – ordered, **Ø** – disordered; **IN** – Tyr80 orienting towards residue 136, **OUT – Tyr80** orienting away from residue 136). *Data taken from reference *(38)*

Extensive rebuilding was required for portions of the structure encompassing loop β3-α3 and adjacent structural elements, where the apo-PaaG^{TT} structure differed from the phasing model. PaaG monomers adopted the canonical crotonase fold of the superfamily with two β-sheets enclosed by six α-helices, as well as a C-terminal helical domain, as previously reported *(38,31)*. In the protein·substrate complex structures, well-defined electron densities were observed indicative of the binding of each CoA-ester substrate; these electron densities were absent in apo-PaaG^{TT} (Figure 3). However, initially-calculated Fo-Fc omit maps for PaaG^{TT}-D136N·**4** displayed poor electron density as a result of the conformational heterogeneity at the terminal moieties of the ligands. To improve the model of the bound ligands, we calculated both 2Fo-Fc maps and POLDER omit maps *(41)* and fitted the ligands into the respective electron densities, which allowed unambiguous identification of substrate positioning. A superimposition of apo-PaaG^{TT} with PaaG^{TT}·**10/12** and PaaG^{TT} D136N·**4** provided root-mean-square deviation values for C_α atoms of 0.42 Å and 0.60 Å, respectively (Supplementary Figure 5). Except for structural elements of the protein near the bound substrates (see below), the overall fold of the all the conformers were virtually identical to apo-PaaG^{TT}. The protein substrate complexes furthermore indicated subtle differences of active site residues upon binding of ligands **4** or **10**/**12**. Notably, the previously unknown C2-C3 double configuration of **4** could be inferred as (*Z*) from our complex structure. Ligand interactions are shown in Supplementary Tables 2 & 3. Interestingly, soaking with stable 2-cyclohexenylacetyl-CoA did not result in significant electron density within the ligand binding site of PaaG^{TT}.

The CoA moieties of both ligands in our complex structures adopt a typical U-form as observed in other Δ^3,Δ^2-enoyl-CoA isomerases with the respective side chains embedded in a hydrophobic site. In contrast to typical Δ^3,Δ^2-enoyl-CoA isomerase substrates such as **9**, the conversion of **2** is exceptional but can be rationalized by considering the known spontaneous and reversible electrocyclic rearrangement of 1,2-epoxybenzene moieties to their oxepin tautomers *(42)*. Hence, **3** is most likely spontaneously formed from **2** (Figure 1A), which is then enzymatically converted to **4**. *In vitro*, the observed reversible PaaG-mediated equilibrium lies on the side of **4** over **2**/**3** *(2)*. Although physiological conditions (i.e. watery solution with high dielectric constant) and the lack of a conjugated α-substitution should favor **2** over **3** *(42)*, PaaG

may stabilize and process the oxepin tautomer in the active site, as the geometry of the planar **3** backbone more closely resembles typical 3,4-enoyl-CoA substrates. Notably, based on our kinetic analyses, PaaG^{TT} (in contrast to PaaG^{PY2}) appears to be significantly better adapted for processing of **2**/**3** rather than **9**. While a structure of PaaG^{PY2} for direct comparison between the two homologous enzymes is currently lacking, we speculate that this substrate preference in PaaG^{TT} proved advantageous in the course of evolution due to the instability and toxicity of **2**, which is exacerbated under thermophilic conditions. It cannot be ruled out, however, that another isomerase is responsible for the isomerization of **9** into **10** in *T. thermophilus*.

Figure 3. Polder OMIT maps (contoured at 3σ above the mean) of (**A**) PaaG^{TT}-D136N•**4** (PDB ID: 6SLA), (**B**) PaaG^{TT}•**10**/**12** (PDB ID: 6SLB), and (**C**) apo-PaaG^{TT} (PDB ID: 6SL9). The unbiased maps allowed placement of the ligands within the electron density. For unsoaked apo-PaaG^{TT}, water molecules and spurious density could be observed. Note that the distance and orientation of residue 136 to the C2 and C4 atoms of the ligand in 6SLA differs due to replacement of the catalytic aspartate residue with asparagine, which adopts a different conformation.

Critical Interactions and Active Site Adaptations of the PaaG Complex Structures

In both protein·substrate complexes, the adenine of the CoA moiety stacks (π-π interaction) with the phenolic ring of the highly-conserved Phe243 *(38)* from the adjacent monomer and is located at the bottom of a well-defined open binding pocket (site 1) (Supplementary Figure 6). CoA binding also involves a salt bridge of the diphosphate moiety with Arg55, as well as hydrogen bonds with Ala59, Glu61 and Leu63 and other non-hydrogen bond interactions (Supplementary Figure 6). In contrast, the acyl moieties of the ligands (both **4** and **10**/**12**) were oriented towards a shallow active site (site 2), which is mostly enclosed by hydrophobic residues. Notably, the main chain amide groups of Gln61 and Ala105 at site 2 participate in H-bonding with the thioester carbonyl of both ligands and are thus ideally positioned to stabilize the thioester enolate transition state (Figure 3). Our mutagenesis studies furthermore suggested a catalytic role for D136 in PaaG^{TT}. Indeed, this residue is positioned in close proximity to C2 and C4 of both ligands **4** and **10**/**12**, with distances between 2.8 Å and 4.1 Å (Figure 4), fully consistent with its envisaged role as proton relay. The carboxylic group of **10**/**12** weakly hydrogen bonds with the Tyr73 side chain (distance of 3.5 Å), thus promoting ligand binding in the hydrophobic site 2.

A comparison of the active-sites of apo-PaaG^{TT}, PaaG^{TT}-D136N·**4** and PaaG^{TT}·**10**/**12** via superimposition of the structures revealed a significant plasticity of the loop β3-α3 residues (residues 66-74). In PaaG^{TT}·**10**/**12**, this loop moved inward compared to the apo form and participates in substrate binding, whereas the density for this loop including Tyr73 was missing in PaaG D136N·**4** and thereby provided space for the bulky oxepin ring (Figure 4, Supplementary Figure 6). In addition to loop β3-α3 flexibility, a displacement of the Tyr80 side chain by around 10 Å resulted in two distinct conformations, as previously observed *(38)*. Interestingly, while the Tyr80 "OUT" conformation was found for apo-PaaG^{TT}, the Tyr80 moved to the "IN" conformation for both protein·substrate complexes, thereby forming a lid over the ligands and furthermore establishing a hydrogen-bond with the side-chain of Gln61 (Figure 3). This closing of the active site was accompanied by the expulsion of water (Supplementary Figure 6). When replaced with phenylalanine in PaaG^{TT}-Y80F, the enzyme showed reduced activity for the conversion of **12** and **2**/**3**, whereas a dual variant PaaG^{TT}-Y80F/D136N exhibited only residual activity for **2**/**3** and did not convert **12** (Table 1). Hence, mutagenesis, enzyme kinetics, and structural data imply an important role for the mobile Tyr80. Ligand binding (**4** as well as **12**) triggers a conformational change of Tyr80 that closes up the active site and displaces water. We speculate that a water-free active site is likely relevant to prevent undesired hydratase activity. Such a side reaction seems plausible, as the functionality of both enoyl-CoA isomerases, as well as structurally-related hydratases, relies on the stabilization of thioester enolate transition states via an oxyanion hole. Consequently, the β-

carbons of product **10** or other 2,3-enoyl-CoAs are susceptible to nucleophilic attack when bound in the active site. By excluding water, PaaG may thus avoid unspecific hydration to (*R*)-3-hydroxyadipoyl-CoA that cannot be further processed by (*S*)-specific 3-hydroxyacyl-CoA dehydrogenases (PaaH in the **1** catabolic pathway). In addition to this functionality, Tyr80 acts as H-bond donor for the carbonyl of the Glu61 side chain (Figure 3), whose main chain NH group stabilizes the enolate transition state. Hence, the H-bonding interaction of Glu61 with Tyr80 likely promotes the active site closure and water expulsion.

These structural adaptations, i.e. the independent movements of two segments (Tyr80 side chain and loop β3-α3) of the active center, apparently achieve the relaxed substrate specificity and facilitate catalysis. From an evolutionary point of view, PaaG may derive from a conventional Δ^3,Δ^2-enoyl-CoA isomerase recruited from fatty acid catabolism and may have conceivably been selected for aromatic degradation because of flexible structural elements that allow the accommodation of bulkier ring substrates.

Figure 4. Overall structure and active site of PaaG^{TT}. (**A**) Superposition of apo-PaaG^{TT} (grey), PaaG^{TT}-D136N•**4** chain A (green), PaaG^{TT}•**10**/**12** (blue). (**B**, **C**, **D**) Inlets showing the respective enlarged active sites. Catalytic residues and ligands are represented as stick models. Distances, e.g., between the catalytic Asp136 and the C2 and C4 atoms of the ligands are indicated in Å. The mobile Tyr80 closes the active site upon substrate binding and expels water. To accommodate **4**, loop β3-α3 opens up and thereby provides space for the bulky ring.

PaaG Restricts the Motional Flexibility of Bound Ligands for Stereochemical Control

To the best of our knowledge, the structural requisites that govern the stereochemistry of Δ^3,Δ^2-enoyl-CoA isomerases have not been clearly established. We thus looked into structural factors in PaaG^{TT} that may control the stereochemistry of the isomerization of **9** to **10** resulting in a *trans*-2,3 configuration, as observed for other Δ^3,Δ^2-enoyl-CoA isomerases. We propose that PaaG^{TT} and related isomerases may constrain the motional flexibility of their substrates and thereby preclude formation of *cis*-2,3 side products, which would arise from (re-)protonation of a bent thioester enolate transition state (Figure 5A). To investigate that, we modelled bent transition state intermediates into the active site of PaaG^{TT} and aligned the respective CoA-moieties and C1–C2 axes with the experimentally observed PaaG^{TT}•**10**/**12** complex structure, while rotating the C2–C3 bonds. Distances between the catalytic D136 side chains and the respective displaced C4 atoms of the conformers remained modest (3.7 – 4.4 Å). On the other hand, the modelling clearly revealed steric clashes with the protein backbone, thus allowing only the elongated conformers to bind (Figure 5BC). A modeling in the active site of multifunctional enzyme, type-1 (MFE1) *(33)* revealed similar steric clashes with the protein backbone (Supplementary Figure 7). These results suggest that a confined active site may be a key determinant for stereochemical control by Δ^3,Δ^2-enoyl-CoA isomerases in order to steer the formation of *trans*-2,3-enoyl-CoAs, which are also energetically favored over the respective *cis*-isomers. In addition, the placement of the catalytic aspartate (D136) may contribute to the regiospecificity, although distances between the D136 side chain and the C4-atom of the substrates in the hypothetical bent states are only marginally different to the experimentally observed ones (Figure 4).

Figure 5. (**A**) Possible conformations of PaaG's native substrate **9** in enzyme free environment (top). The thioester enolates, following deprotonation, represent the transition states (middle), which are converted to the products (bottom). If the transition state adopts a bent conformation (red boxes), the undesired *cis*-2,3 product would be formed rather than the observed *trans*-2,3 (blue boxes). R = CH_2COOH. (**B, C**) PaaG^{TT} suppresses the bent conformation of the transition state through a confined active site, thereby steering the exclusive formation of *trans*-2,3-didehydroadipoyl-CoA (**10**). Modeled bent *cis*-1,2, *cis*-3,4 transition state binding-modes are shown as yellow sticks (**B**) and modeled bent *trans*-1,2, *cis*-3,4 transition state binding-modes as green sticks (**C**). Both transition state models are aligned along the CoA-moieties and C1-C2 axes with the experimentally observed **10**/**12**

(pink sticks). Red spheres represent steric clashes of transition states with the protein. The C2 and C4 atoms are highlighted as spheres with indicated distances to the catalytic D136 side chain.

Conclusion

In this work we biochemically and structurally characterized the unusual isomerase PaaG and verify a Δ^3,Δ^2-enoyl-CoA isomerases-like mechanism. Our mechanistic and structural studies of the wild type and the enzyme variants furthermore strongly suggest a catalytic aspartate (D136) side chain that is ideally situated to act as proton shuttle, similar to structurally related isomerases. The installment of an α-β double bond in **4** by PaaG subsequently enables facile β-hydration, ring cleavage and further β-oxidation-like steps. Hence, PaaG acts as crucial mediator between aromatic degradation and β-oxidation. In addition to the previously confirmed conversion of **2**/**3** into **4** *(2)*, we verify a second role for PaaG in the **1** catabolic pathway, where PaaG catalyzes the isomerization of **9** into **10** and thus processes two structurally-distinct substrates. Our data furthermore grants insight into how control of *trans*-2,3 stereospecificity is exerted by $PaaG^{TT}$. We show that $PaaG^{TT}$ (and related enzymes) feature a confined substrate binding site and thereby preclude formation of *cis*-2,3 side products that would result from bent thioester enolate transition states.

Interestingly, the PaaG product **4** is not only degraded to acetyl-CoA and succinyl-CoA, but most likely also serves as precursor for unusual primary metabolites (ω-cycloheptyl fatty acids *(15)*) as well as secondary metabolites *(11)* known to have antimicrobial, anticancer, and antiviral activities, i.e. tropone natural products such as **8** *(20,16,43,21,19)* or roseobacticides *(28,27,26)*) (Figure 1A). Tropones and derivatives are produced by numerous bacteria including predominant marine *Roseobacter* sp. and are also detected among the bacterial volatiles *(44–46)*). Moreover, **8** has been shown to not only act as antibiotic, but also as bacterial quorum-sensing signal *(47,17)*. These compounds furthermore appear to play a central role in marine symbiotic relationships of bacterial producers with oysters, sponges, algae and corals by warding off pathogens *(27,22,48,23)* and likely have a pivotal role in structuring coral-associated bacterial communities *(48)*. Moreover, **8** is a promising antibiotic, e.g., for use in aquacultures, as resistance mechanisms develop slowly, are conferred on a low level, and disappear rapidly *(23,49,50)*. PaaG and the extraordinary isomerization of **2**/**3** to **4** is thus a key functionality for formation of these ecologically and pharmaceutically interesting metabolites.

In summary, we characterized the bacterial PaaG in detail and for the first time elucidated structures of a Δ^3,Δ^2-enoyl-CoA isomerase in complex with its native ligands. Our data provide a rationale for the observed substrate flexibility as well as the enzymatic control of stereospecificity. Hence, our findings also shed new light onto the general Δ^3,Δ^2-enoyl-CoA isomerase type, which are most commonly involved in the β-oxidation of unsaturated fatty acids that carry a double bond at an odd position. In the future, PaaG may be a prime candidate for biotechnological applications and exploited for *in vitro* or *in vivo* production and bioengineering of tropone natural products.

Methods

Cloning and Mutagenesis

To heterologously produce PaaG from *Thermus thermophilus*, the gene was amplified by PCR (oligonucleotides in Supplementary Table 1) from genomic DNA. The PCR product was isolated and cloned into the pET His6 TEV LIC cloning vector (Addgene). For site-directed mutagenesis, primers with single-point-mutation (Supplementary Table 4) were used to create the mutants $PaaG^{TT}$ Y80F, D136N and Y80F/D136N. Sequence mutations were confirmed by DNA sequencing (Eurofins Genomics).

Protein Expression and Purification

PaaG from *Pseudomonas* sp. Y2 was produced in *E. coli* BL21 (DE3) and purified as described previously *(2)*. The isolated protein was stored with 30 % glycerol at -20°C. For overexpression, the recombinant plasmid pET His6 TEV LIC-*paaG*^{TT} was transformed into *E. coli* BL21 (DE3) (Thermo Fisher Scientific). Liquid cultures were grown shaking at 37°C until an OD_{600} of 0.5-0.6 was reached. Then, the temperature was lowered to 18°C and protein production was induced by adding IPTG to a final concentration of 100 µM. After 19-22 hours, the cells were harvested by centrifugation at 3220 g and 4°C for 15 minutes. Cell pellets were stored at –20°C or directly resuspended in buffer A (20 mM Tris-HCl, 100 mM KCl, 1 mg mL^{-1} DNase I, pH 8.0) for protein isolation. The suspension was sonicated 3 times (0.5 sec on, 2.5 sec off, 40 % amplitude, 5 minutes pause) on ice, incubated for 15 minutes in a 65°C water bath, and centrifuged (100000 x g) at 4°C for 1 h. The supernatant was directly applied to a FF HisTrap 5 mL column (GE Healthcare) by FPLC (Äkta Pure, GE Healtcare), washed and eluted with buffer B (20 mM Tris-HCl, 100 mM KCl, 500 mM imidazole, pH 8.0). After elution, the fractions with high protein concentration were pooled and desalted with a HiTrap-column (GE Healthcare). For crystallization, the polyhistidine-tags of PaaG^{TT} wt and the PaaG^{TT}-D136N variant were cleaved off by digestion with TEV protease. For that, the protein fractions were pooled and concentrated using a 10 kDa MW cut-off MACROSEP spin column (Pall Cooperation) to a volume of 4 mL and supplemented with 1 mM dithiothreitol (DTT), 0.5 mM EDTA (pH 8.0) and 1.5 mg TEV-His protease. The mixture was incubated over night at 4°C and then applied to a FF HisTrap column. The flow-through was collected that contained the protein without tag. The purity of the protein was then increased by size exclusion chromatography utilizing a HiLoad 16/600 Superdex 200 pg column (GE Healthcare) equilibrated with buffer C (20 mM Tris-HCl, 150 mM NaCl, 1 mM DTT pH 8.0) and connected to a FPLC system. The eluted protein was stored with 20 % (v/v) glycerol at -20 °C. The purity of the eluted protein was confirmed by SDS-PAGE.

Specific Activities for Unstable 1,2-Epoxyphenylacetyl-CoA (2) and *cis*-3,4-Didehyroadipoyl-CoA (9).

A solution of 50 mM Tris-HCl pH 8.0, 0.3 mM phenylacetyl-CoA, 1 mM NADPH and 1 mg mL^{-1} PaaABCE was prepared. The premix was incubated at 30°C for 3 minutes. The isomerization reaction was then started by the addition of PaaG (1 nM PaaG^{TT} wt, 2 nM PaaG^{TT} Y80F, 20 nM PaaG^{TT} D136N, 10 nM PaaG^{TT} Y80F/D136N or 0.5 nM PaaG^{PY2} wt). To calculate the specific activity, the formed **4** over time was quantified by HPLC using a standard curve. Accordingly, samples were withdrawn at varying time points and quenched with 100 % (v/v) ice cold MeOH. After centrifugation for 20 min at 18,000 × g, MeOH was removed by speed vac and samples analyzed by HPLC. For **9**, the specific activity was also determined via a coupled assay and quantified by UPLC-HRMS. A solution of 50 mM Tris-HCl pH 8.0, 0.3 mM 3-oxo-5,6-didehydrosuberyl-CoA, 0.45 mM CoA and 0.2 µM PaaJ was prepared and incubated at 30°C for 10 minutes. The isomerization reaction was then started by the addition of PaaG^{TT} wt (800 nM, 400 nM, 160 nM) or PaaG^{PY2} wt (25 nM, 10 nM, 2,5 nM). After 1 min, the reaction was stopped by addition of 200 % (v/v) ice-cold MeOH. After centrifugation for 2 x 20 min at 18,000 × g, MeOH was removed by speed vac and samples were analyzed by UPLC-HRMS.

Photometric Assays for *trans*-3,4-Didehyroadipoyl-CoA

The kinetic parameters for *trans*-3,4-didehyroadipoyl-CoA were determined photometrically using a UV-1650PC Shimadzu spectrophotometer. The isomerization of *trans*-3,4-didehyroadipoyl-CoA to *trans*-2,3-didehyroadipoyl-CoA was quantified by measuring the increase of absorption at 260 nm because of different extinction coefficients (16.4 cm^{-1} mM^{-1} for saturated acyl-CoAs; 22.4 cm^{-1} mM^{-1} for unsatured enoyl-CoAs) *(39)*. Reaction rates were then calculated according to Beer–Lambert law. Because of the absorption limit of the detector, a 1 mm cuvette (Type 110-QS, 1 mm, Hellma) was used for concentrations of 200 µM substrate

and above and a 10 mm cuvette (Type 105.205-QS, Hellma) for 100 µM and below. The reaction mixtures contained 10 µM, 20 µM, 50 µM, 100 µM, 200 µM or 1 mM *trans*-3,4-didehyroadipoyl-CoA in 50 mM Tris-HCl pH 8.0. The reactions were started by addition of a sufficient quantity of PaaG that allowed measuring the linear increase in absorption. The slope of the absorption was read out by the software (UV Probe 2.43, Shimadzu).

Chemical and Enzymatic Synthesis of CoA-Esters

Trans-3,4-didehydroadipoyl-CoA was chemically synthesized from free acid and CoA via activation of the carboxyl group by N,N'-dicyclohexylcarbodiimide and esterification to the respective succinimide ester intermediates *(51)*. Accordingly, *trans*-2-butene-1,4-dicarboxylic acid (abcr, Germany) (0.75 g, 5 mmol) and 0.58 g N-hydroxysuccinimid were dissolved in 25 mL water-free dioxane. A solution of dicyclohexylcarbodiimid (1.55 g, 7.5 mmol) in 5 mL dioxane was dripped to the starter mixture over 30 min and the reaction mixture stirred overnight. The filtrate was freeze dried and stored at -20 °C. For the esterification, 20 mL hydrogencarbonat solution (100 mM, pH 8) was mixed with 50 mg succinimid ester and Coenzyme A (50 mg, 64 µmol) under anaerobic conditions. The consumption of free CoA was checked with Ellmans' reagant. After completion of the reaction the pH was adjusted to 3.5 with 20 % acetic acid. After reduction of the volume, the CoA-esters were purified via HPLC. Phenylacetyl-CoA was synthesized via the same method beginning with phenylacetic-succinimid (inherited from Georg Fuchs) and free CoA. Cyclohexenyliden-CoA was chemically synthesized of 2-(cyclohex-1-en-1-yl)acetic acid (Enamine, Ukraine) (3.8 mg, 26.8 µmol), 1-Hydroxybenzotriazole (3.6 mg, 26.8 µmol), tetramethyluronium tetrafluoroborate (8.6 mg, 26.8 µmol), N-ethyldiisopropylamine (16 µL, 12.2 mg, 94 µmol) and Coenzyme A trilithium salt (20 mg, 24.4 µmol) according to *(52)*. All chemical syntheses were conducted at room temperature. Compounds **4** and **6** were enzymatically synthesized *in vitro* in large scale in 20 mL assays and purified by semi-preparative HPLC. For **4** formation, assays contained 20 µg PaaABCE, 0.4 µg $PaaG^{PY2}$ wt, 1 mM NADPH, 0.5 mM Pa-CoA in 50 mM Tris-HCl pH 8.0. Compounds were then purified via semi-preparative RP-HPLC and lyophilized.

Ultra/High Performance Liquid Chromatography

Compounds were isolated using reverse-phase High Performance Liquid Chromatography (RP-HPLC) on a 1100 series chromatographic system (Agilent Technologies) with a semi-preparative C18-E column (Nucleodur C18e 250/10, Machery-Nagel). For activity tests, the column was developed at a flow rate of 4.5 mL min^{-1} by a linear gradient from 2 % acetonitrile in 10 mM ammonium acetate (pH 6.8) to 100% acetonitrile within 20 min, after 2 min at isocratic conditions with 2% acetonitrile. For isolation of chemically produced compounds or enzymatically produced **6**, a flow rate of 3.5 mL min^{-1} with the same gradient but with ammonium acetate at pH 4.5 was used.

Liquid Chromatography-Mass Spectrometry

For identification of intermediates, enzymatic assays were analyzed by Waters Acquity I-class UPLC (Waters C-18 HSS T3 column, 2.1 mm x 100 mm, 1.8 µm particle size) coupled to a Waters Acquity photo diode array detector (Waters) and a Waters Synapt G2-S*i* HDMS electrosprayionization (ESI)/quadrupole time-of-flight (Q-TOF) system. Two minutes after injection, the initial concentration of 2 % acetonitrile in ammonium acetate (pH 4.5) at a flow rate of 0.2 mL min^{-1} was increased via a linear gradient to 30 % acetonitrile in 9 min. CoA esters were measured in MS positive mode with a capillary voltage of 1.5 kV, 100 °C source temperature, 300°C desolvation temperature, 600 L min^{-1} N2 desolvation gas flow. Collision induced dissociation of precursor ions was performed using a collision energy ramp from 10 to 40 V.

Circular Dichroism Spectroscopy

Circular dichroism (CD) of PaaG^{TT} wt and variants were recorded in a 0.2 mm path length cuvette at 25°C with a Jasco J-810 spectropolarimeter (Jasco, Easton, MD, USA) equipped with a Peltier temperature controller. Protein samples were dissolved in 10 mM sodium phosphate buffer (pH 8.0). Protein concentration was determined by the Bradford method. Instrumental parameters for measurement of the CD spectra were: 190-300 nm measurement range, 1 nm band width, standard sensitivity, 200 nm/min of scanning speed. Analysis method: Three spectra for each enzyme variant as well as the buffer were measured and averaged. To receive the CD spectra, the buffer was subtracted and the received CD spectra were normalized to mean residue ellipticity θ_{MRW} (deg x cm^2 x dmol^{-1}).

Crystallization, X-ray Data Collection and Processing

Crystallization screens were conducted using the sitting drop vapor diffusion method matching the published conditions. After screening and optimization with various precipitants, crystallizations were set up manually using the vapor diffusion sitting drop method with 48-well plates. The reservoir solution contained 50 mM KH_2PO4, pH 4.5, 20-22% PEG 3350, 3% (w/v) non-detergent sulfobetain (NDSB-201) and 20% glycerol (v/v) at 25°C. The drops were set up at a 1:1 ratio of protein to reservoir solution and incubated at 25 °C. Co-crystallization trials with substrates oxepin-CoA (**4**) and *trans*-3,4-didehydroadipoyl-CoA (**11**) were unsuccessful, hence crystal soaking was implemented. For PaaG D136N·**4** complex, respective crystals were soaked in a 10 mM solution of **4** for a short period of 2 hours to 4 hours. For PaaG·**10**/**12** complex, a pinch of the compound was sprinkled over the crystals for soaking between 2 and 16 hours. Each crystal was transferred into the reservoir solution, which also acted as cryobuffer, and subsequently flash-cooled to 100 K in a cold nitrogen-gas stream. Crystals diffracted up to 1.27 Å for the apo protein, 1.88 Å for PaaG·**10**/**12**, and up to 2.55 Å for PaaG D136N·**4** and were recorded at the Swiss Light source (Villigen, Switzerland) on beam station PXI at 100 K. Cryo cooling was carried out prior to X-ray data collection, after stabilizing the crystals in mother liquor cryoprotectant. The datasets were processed by XDS in $P2_13$ (a = b = c = 88.02 for the 1.27 Å dataset and a = b = c = 88.45 for the 1.88 Å dataset) and $P2_1$ (a = 76.16 b = 73.05 c = 130.30, β = 92.5° for the 2.55 Å dataset). The X-ray diffraction reflections were merged and scaled using SCALA.

Structure Determination, Model Building and Refinement

Initial phases for the apo structure at 1.27 Å and PaaG·**10**/**12** complex at 1.88 Å (form II), and PaaG·**4** complex at 2.55 Å (form III) were calculated by molecular replacement using PDB code 3HRX chain A of apo PaaG (space group $P2_12_12_1$, form I) as the search model and PHASER as implemented in PHENIX. The missing residues from 66 to 74 in the original published PaaG structure were built based on the electron density map of the PaaG apo structure at 1.27 Å. Electron density for ligands **4** and **10**/**12** were observed at the active site in their respective complexes and these ligands were modeled. To ensure that stereochemical restraints imposed on the ligands during the refinement process had not biased the geometry of the resulting models in the active site, restraints were removed from the ligands and a subsequent round of simulated annealing refinement was carried out in PHENIX *(53)*. For omit map calculations, the Polder OMIT maps tool was used. Further refinement and model building were performed using the PHENIX software suite and COOT *(54)*. Statistics for data reduction, model refinement, and model quality are summarized in Table 1. The model is complete for residues 1–254 with the exception of residues 66–74, in external loops between helices α2 to α3 that could not be modeled because of conformational heterogeneity.

Figure Generation and Data Deposition

Graphic images were generated using PyMOL*(55)* and representations of substrate binding were generated using the academic free version of Discovery Studio Visualizer *(56)*.

Accession codes

The atomic coordinates and structure factors (PDB codes 6SL9, 6SLA, 6SLB) were deposited in the Protein Data Bank.

Associated Content

Supporting Information Available: This material is available free of charge via the Internet.

Additional data on enzyme kinetics, CD spectroscopy, X-ray crystallography (including refinement statistics), and list of oligonucleotides (PDF).

Author Information

Corresponding Author: *E-mail: robin.teufel@zbsa.uni-freiburg.de.

ORCID:
Robin Teufel: 0000-0001-5863-7248

Author Contributions: M.S. planned and conducted mechanistic experiments and analyzed and interpreted data; R.S.B. planned and conducted X-ray crystallography experiments and analyzed and interpreted data; R.T. designed research, analyzed and interpreted data and wrote the manuscript. M.S. and R.S.B. contributed equally to the work.

Notes: The authors have no conflict of interest to declare.

Acknowledgements: We thank G. Fuchs in whose group this project was initiated and S. Lüdeke for assisting with CD spectroscopy. We thank T. Takashi from the Swiss Light Source (SLS), Villigen (CH) for technical support.

Funding: This work was supported by a DFG grant awarded to R.T. (TE 931/2-1). The research leading to these results has received funding from the European Union's Horizon 2020 research and innovation programme under grant agreement n.° 730872, project CALIPSOplus.

References

1. Fuchs, G., Boll, M., and Heider, J. (2011) Microbial degradation of aromatic compounds — from one strategy to four, *Nat. Rev. Microbiol. 9,* 803–816.
2. Teufel, R., Mascaraque, V., Ismail, W., Voss, M., Perera, J., Eisenreich, W., Haehnel, W., and Fuchs, G. (2010) Bacterial phenylalanine and phenylacetate catabolic pathway revealed, *Proc. Natl. Acad. Sci. U S A 107,* 14390–14395.
3. Olivera, E. R., Miñambres, B., García, B., Muñiz, C., Moreno, M. A., Ferrández, A., Díaz, E., García, J. L., and Luengo, J. M. (1998) Molecular characterization of the phenylacetic acid catabolic pathway in Pseudomonas putida U: the phenylacetyl-CoA catabolon, *Proc. Natl. Acad. Sci. U S A 95,* 6419–6424.
4. Navarro-Llorens, J. M., Patrauchan, M. A., Stewart, G. R., Davies, J. E., Eltis, L. D., and Mohn, W. W. (2005) Phenylacetate catabolism in Rhodococcus sp. strain RHA1: a central pathway for degradation of aromatic compounds, *J. Bacteriol. 187,* 4497–4504.
5. Luengo, J. M., García, J. L., and Olivera, E. R. (2001) The phenylacetyl-CoA catabolon: a complex catabolic unit with broad biotechnological applications, *Mol. Microbiol. 39,* 1434–1442.
6. Ismail, W., El-Said Mohamed, M., Wanner, B. L., Datsenko, K. A., Eisenreich, W., Rohdich, F., Bacher, A., and Fuchs, G. (2003) Functional genomics by NMR spectroscopy. Phenylacetate catabolism in Escherichia coli, *Eur. J. Biochem. 270,* 3047–3054.

7. Ferrández, A., Miñambres, B., García, B., Olivera, E. R., Luengo, J. M., García, J. L., and Díaz, E. (1998) Catabolism of phenylacetic acid in Escherichia coli. Characterization of a new aerobic hybrid pathway, *J. Biol. Chem. 273,* 25974–25986.
8. Bartolomé-Martín, D., Martínez-García, E., Mascaraque, V., Rubio, J., Perera, J., and Alonso, S. (2004) Characterization of a second functional gene cluster for the catabolism of phenylacetic acid in Pseudomonas sp. strain Y2, *Gene 341,* 167–179.
9. Rather, L. J., Knapp, B., Haehnel, W., and Fuchs, G. (2010) Coenzyme A-dependent aerobic metabolism of benzoate via epoxide formation, *J. Biol. Chem. 285,* 20615–20624.
10. Teufel, R., Friedrich, T., and Fuchs, G. (2012) An oxygenase that forms and deoxygenates toxic epoxide, *Nature 483,* 359–362.
11. Teufel, R., Gantert, C., Voss, M., Eisenreich, W., Haehnel, W., and Fuchs, G. (2011) Studies on the mechanism of ring hydrolysis in phenylacetate degradation: a metabolic branching point, *J. Biol. Chem. 286,* 11021–11034.
12. Pribytkova, T., Lightly, T. J., Kumar, B., Bernier, S. P., Sorensen, J. L., Surette, M. G., and Cardona, S. T. (2014) The attenuated virulence of a Burkholderia cenocepacia paaABCDE mutant is due to inhibition of quorum sensing by release of phenylacetic acid, *Mol. Microbiol. 94,* 522–536.
13. Erb, T. J., Ismail, W., and Fuchs, G. (2008) Phenylacetate metabolism in thermophiles: characterization of phenylacetate-CoA ligase, the initial enzyme of the hybrid pathway in Thermus thermophilus, *Curr. Microbiol. 57,* 27–32.
14. Grishin, A. M., Ajamian, E., Tao, L., Zhang, L., Menard, R., and Cygler, M. (2011) Structural and functional studies of the Escherichia coli phenylacetyl-CoA monooxygenase complex, *J. Biol. Chem. 286,* 10735–10743.
15. Moore, B. S., Walker, K., Tornus, I., Handa, S., Poralla, K., and Floss, H. G. (1997) Biosynthetic Studies of omega-Cycloheptyl Fatty Acids in Alicyclobacillus cycloheptanicus. Formation of Cycloheptanecarboxylic Acid from Phenylacetic Acid, *J. Org. Chem. 62,* 2173–2185.
16. Bentley, R. (2008) A fresh look at natural tropolonoids, *Nat. Prod. Rep. 25,* 118–138.
17. Berger, M., Neumann, A., Schulz, S., Simon, M., and Brinkhoff, T. (2011) Tropodithietic acid production in Phaeobacter gallaeciensis is regulated by N-acyl homoserine lactone-mediated quorum sensing, *J. Bacteriol. 193,* 6576–6585.
18. Berger, M., Brock, N. L., Liesegang, H., Dogs, M., Preuth, I., Simon, M., Dickschat, J. S., and Brinkhoff, T. (2012) Genetic analysis of the upper phenylacetate catabolic pathway in the production of tropodithietic acid by Phaeobacter gallaeciensis, *Appl. Environ. Microbiol. 78,* 3539–3551.
19. Brock, N. L., Nikolay, A., and Dickschat, J. S. (2014) Biosynthesis of the antibiotic tropodithietic acid by the marine bacterium Phaeobacter inhibens, *Chem. Commun. 50,* 5487–5489.
20. Chen, X., Xu, M., Lü, J., Xu, J., Wang, Y., Lin, S., Deng, Z., and Tao, M. (2018) Biosynthesis of Tropolones in Streptomyces spp.: Interweaving Biosynthesis and Degradation of Phenylacetic Acid and Hydroxylations on the Tropone Ring, *Appl. Environ. Microbiol.* Epub 2018. DOI: 10.1128/AEM.00349-18.
21. Geng, H., Bruhn, J. B., Nielsen, K. F., Gram, L., and Belas, R. (2008) Genetic dissection of tropodithietic acid biosynthesis by marine roseobacters, *Appl. Environ. Microbiol. 74,* 1535–1545.
22. Harrington, C., Reen, F. J., Mooij, M. J., Stewart, F. A., Chabot, J.-B., Guerra, A. F., Glöckner, F. O., Nielsen, K. F., Gram, L., Dobson, A. D. W., Adams, C., and O'Gara, F. (2014) Characterisation of non-autoinducing tropodithietic Acid (TDA) production from marine sponge Pseudovibrio species, *Mar. Drugs 12,* 5960–5978.
23. Zhao, W., Dao, C., Karim, M., Gomez-Chiarri, M., Rowley, D., and Nelson, D. R. (2016) Contributions of tropodithietic acid and biofilm formation to the probiotic activity of Phaeobacter inhibens, *BMC Microbiol. 16,* 1.
24. Kintaka, K., Ono, H., Tsubotani, S., Harada, S., and Okazaki, H. (1984) Thiotropocin, a new sulfur-containing 7-membered-ring antibiotic produced by a Pseudomonas sp, *J. Antibiot. 37,* 1294–1300.
25. Guo, H., Roman, D., and Beemelmanns, C. (2018) Tropolone natural products, *Nat. Prod. Rep.*
26. Seyedsayamdost, M. R., Carr, G., Kolter, R., and Clardy, J. (2011) Roseobacticides: small molecule modulators of an algal-bacterial symbiosis, *J. Am. Chem. Soc. 133,* 18343–18349.
27. Seyedsayamdost, M. R., Wang, R., Kolter, R., and Clardy, J. (2014) Hybrid biosynthesis of roseobacticides from algal and bacterial precursor molecules, *J. Am. Chem. Soc. 136,* 15150–15153.
28. Wang, R., Gallant, É., and Seyedsayamdost, M. R. (2016) Investigation of the Genetics and Biochemistry of Roseobacticide Production in the Roseobacter Clade Bacterium Phaeobacter inhibens, *mBio 7,* e02118.
29. Nogales, J., Macchi, R., Franchi, F., Barzaghi, D., Fernández, C., García, J. L., Bertoni, G., and Díaz, E. (2007) Characterization of the last step of the aerobic phenylacetic acid degradation pathway, *Microbiology (Reading, England) 153,* 357–365.
30. Holden, H. M., Benning, M. M., Haller, T., and Gerlt, J. A. (2001) The crotonase superfamily: divergently related enzymes that catalyze different reactions involving acyl coenzyme a thioesters, *Acc. Chem. Res. 34,* 145–157.

31. Grishin, A. M., Ajamian, E., Zhang, L., Rouiller, I., Bostina, M., and Cygler, M. (2012) Protein-protein interactions in the β-oxidation part of the phenylacetate utilization pathway: crystal structure of the PaaF-PaaG hydratase-isomerase complex, *J. Biol. Chem. 287,* 37986–37996.
32. Engel, C. K., Kiema, T. R., Hiltunen, J. K., and Wierenga, R. K. (1998) The crystal structure of enoyl-CoA hydratase complexed with octanoyl-CoA reveals the structural adaptations required for binding of a long chain fatty acid-CoA molecule, *J. Mol. Biol. 275,* 847–859.
33. Kasaragod, P., Schmitz, W., Hiltunen, J. K., and Wierenga, R. K. (2013) The isomerase and hydratase reaction mechanism of the crotonase active site of the multifunctional enzyme (type-1), as deduced from structures of complexes with 3S-hydroxy-acyl-CoA, *FEBS J. 280,* 3160–3175.
34. Partanen, S. T., Novikov, D. K., Popov, A. N., Mursula, A. M., Kalervo Hiltunen, J., and Wierenga, R. K. (2004) The 1.3Å Crystal Structure of Human Mitochondrial Δ3-Δ2-Enoyl-CoA Isomerase Shows a Novel Mode of Binding for the Fatty Acyl Group, *J. Mol. Biol. 342,* 1197–1208.
35. Zhang, D., Yu, W., Geisbrecht, B. V., Gould, S. J., Sprecher, H., and Schulz, H. (2002) Functional characterization of Delta3,Delta2-enoyl-CoA isomerases from rat liver, *J. Biol. Chem. 277,* 9127–9132.
36. Mursula, A. M., van Aalten, D. M.F., Hiltunen, J.K., and Wierenga, R. K. (2001) The crystal structure of Δ3-Δ2-enoyl-CoA isomerase, *J. Mol. Biol. 309,* 845–853.
37. Crooks, G. P., and Copley, S. D. (1994) Purification and characterization of 4-chlorobenzoyl CoA dehalogenase from Arthrobacter sp. strain 4-CB1, *Biochemistry 33,* 11645–11649.
38. Kichise, T., Hisano, T., Takeda, K., and Miki, K. (2009) Crystal structure of phenylacetic acid degradation protein PaaG from Thermus thermophilus HB8, *Proteins 76,* 779–786.
39. Peter, D. M., Vögeli, B., Cortina, N. S., and Erb, T. J. (2016) A Chemo-Enzymatic Road Map to the Synthesis of CoA Esters, *Molecules (Basel, Switzerland) 21,* 517.
40. Krissinel, E., and Henrick, K. (2007) Inference of macromolecular assemblies from crystalline state, *J. Mol. Biol. 372,* 774–797.
41. Liebschner, D., Afonine, P. V., Moriarty, N. W., Poon, B. K., Sobolev, O. V., Terwilliger, T. C., and Adams, P. D. (2017) Polder maps: improving OMIT maps by excluding bulk solvent, *Acta Crystallogr. D Struct. Biol. 73,* 148–157.
42. Vogel, E., and Günther, H. (1967) Benzene Oxide-Oxepin Valence Tautomerism, *Angew. Chem. Int. Ed. Engl. 6,* 385–401.
43. Cane, D. E., Wu, Z., and van Epp, J. E. (1992) Thiotropocin biosynthesis. Shikimate origin of a sulfur-containing tropolone derivative, *J. Am. Chem. Soc. 114,* 8479–8483.
44. Rost, R., Haas, S., Hammer, E., Herrmann, H., and Burchhardt, G. (2002) Molecular analysis of aerobic phenylacetate degradation in Azoarcus evansii, *Mol. Genet. Genomics 267,* 656–663.
45. Thiel, V., Brinkhoff, T., Dickschat, J. S., Wickel, S., Grunenberg, J., Wagner-Döbler, I., Simon, M., and Schulz, S. (2010) Identification and biosynthesis of tropone derivatives and sulfur volatiles produced by bacteria of the marine Roseobacter clade, *Org. Biomol. Chem. 8,* 234–246.
46. Citron, C. A., Rabe, P., and Dickschat, J. S. (2012) The scent of bacteria: headspace analysis for the discovery of natural products, *J. Nat. Prod. 75,* 1765–1776.
47. Wilson, M. Z., Wang, R., Gitai, Z., and Seyedsayamdost, M. R. (2016) Mode of action and resistance studies unveil new roles for tropodithietic acid as an anticancer agent and the γ-glutamyl cycle as a proton sink, *Proc. Natl. Acad. Sci. U S A 113,* 1630–1635.
48. Raina, J.-B., Tapiolas, D., Motti, C. A., Foret, S., Seemann, T., Tebben, J., Willis, B. L., and Bourne, D. G. (2016) Isolation of an antimicrobial compound produced by bacteria associated with reef-building corals, *PeerJ 4,* e2275.
49. Rasmussen, B. B., Grotkjær, T., D'Alvise, P. W., Yin, G., Zhang, F., Bunk, B., Spröer, C., Bentzon-Tilia, M., and Gram, L. (2016) Vibrio anguillarum Is Genetically and Phenotypically Unaffected by Long-Term Continuous Exposure to the Antibacterial Compound Tropodithietic Acid, *Appl. Environ. Microbiol. 82,* 4802–4810.
50. Porsby, C. H., Webber, M. A., Nielsen, K. F., Piddock, L. J. V., and Gram, L. (2011) Resistance and tolerance to tropodithietic acid, an antimicrobial in aquaculture, is hard to select, *Antimicrob. Agents Chemother. 55,* 1332–1337.
51. Schachter, D., and Taggart, J. V. (1953) Benzoyl coenzyme A and hippurate synthesis, *J. Biol. Chem. 203,* 925–934.
52. Willistein, M., Haas, J., Fuchs, J., Estelmann, S., Ferlaino, S., Müller, M., Lüdeke, S., and Boll, M. (2018) Enantioselective Enzymatic Naphthoyl Ring Reduction, *Chemistry 24,* 12505–12508.
53. Adams, P. D., Afonine, P. V., Bunkóczi, G., Chen, V. B., Davis, I. W., Echols, N., Headd, J. J., Hung, L.-W., Kapral, G. J., Grosse-Kunstleve, R. W., McCoy, A. J., Moriarty, N. W., Oeffner, R., Read, R. J., Richardson, D. C., Richardson, J. S., Terwilliger, T. C., and Zwart, P. H. (2010) PHENIX: a comprehensive Python-based system for macromolecular structure solution, *Acta Crystallogr. D Biol. Crystallogr. 66,* 213–221.
54. Emsley, P., and Cowtan, K. (2004) Coot: model-building tools for molecular graphics, *Acta Crystallogr. D Biol. Crystallogr. 60,* 2126–2132.

55. The PyMOL Molecular Graphics System, Version 2.0 Schrödinger, LLC.
56. Dassault Systèmes BIOVIA, Discovery Studio Visualizer, v 17.2.0, San Diego: Dassault Systèmes, 2017

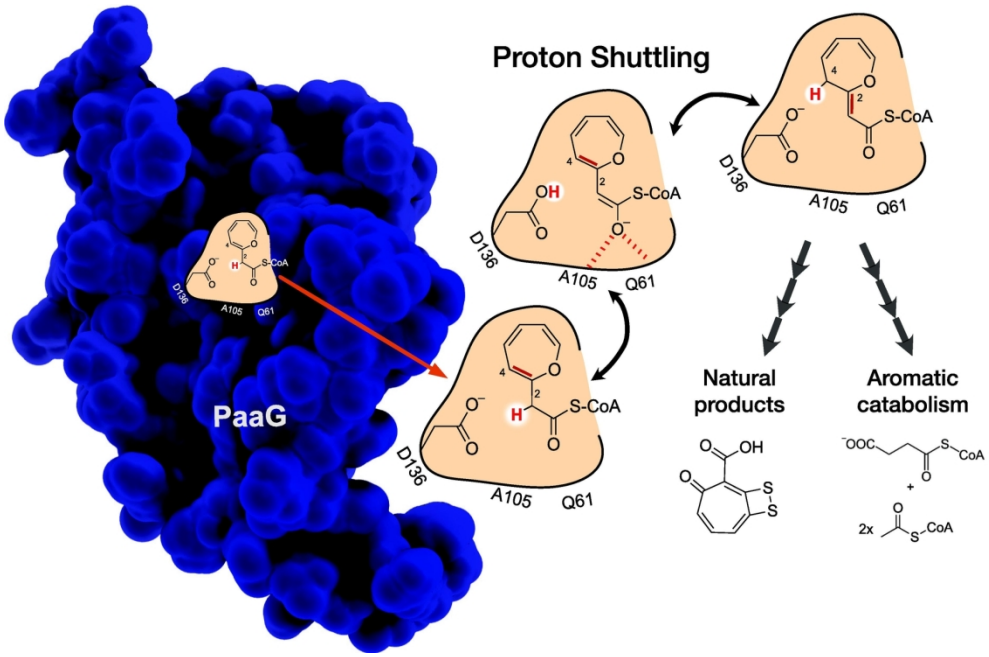

Proton shuttling by PaaG
(graphical abstract)

159x103mm (300 x 300 DPI)